JOURNAL OF PROPULSION AND POWER
Vol. 25, No. 2, March–April 2009

Impulse Generation on Aluminum Target Irradiated with Nd:YAG Laser Pulse in Ambient Gas

Takeharu Sakai*
Nagoya University, Nagoya 464-8603, Japan

DOI: 10.2514/1.37767

Mechanisms of the impulse on an aluminum foil generated through laser ablation with the Nd:YAG laser with a wavelength of 1064 nm are studied by fitting computed results to the time-resolved impulse data measured by using the Velocity Interferometer System for any reflector for different ambient pressures ranging from 10^{-2} to 10^{5} Pa. The computational method used accounts for thermal conduction within the aluminum target, the vaporization process under equilibrium thermodynamics through the Clausius–Clapeyron equation, and the expansion of aluminum ablation jet described by compressible gas dynamics with the laser radiation energy transfer. A constant reflectivity value on the aluminum target surface is used to replicate the time-resolved impulse data. The present study shows that the breakdown of ambient gas and the gas dynamic confinement of an ablation jet are attributed to the impulse generation at higher pressure cases after the laser power peak of the Nd:YAG laser. At lower ambient pressures, the impulse is produced due to the momentum transfer of the aluminum vapor ejected by laser ablation during the laser power peak.

Nomenclature

c = velocity of light, 2.998×10^{8} m/s
D_{N_2} = dissociation energy of N_2, 9.74 eV
e = elementary electrical charge, 1.602×10^{-19} C
H = enthalpy of aluminum target, J/m^3
h = Planck constant, 6.626×10^{-34}
I_{N} = first ionization energy of nitrogen, 14.53 eV
I_{Al} = first ionization energy of aluminum, 5.99 eV
I_{Al^+} = second ionization energy of aluminum, 18.23 eV
I = laser intensity, W/m^2
k = Boltzmann constant, 1.38×10^{-23} J/K or 8.62×10^{-5} eV/K
m = mass of aluminum, kg
n_i = number density of species i, m^{-3}
p = pressure, Pa
Q = partition function
R_g = universal gas constant, 8.314 J/mol $\cdot$ K
R_{sf} = reflectivity
T_{bp} = boiling temperature, K
t = time, s
v = velocity, m/s
x = spatial coordinate, m
z = coordinate within target, m
ΔH_v = heat of vaporization at normal boiling point, kJ/mol
ϵ_D = dissociation energy, J/m^3
ϵ_I = ionization energy, J/m^3
κ = thermal conductivity, W/(m $\cdot$ K), or absorption coefficient, m^{-1}
λ = wavelength, m
τ_{FWHM} = full width at half-maximum of laser power peak, s

Subscripts

$\tilde{\mathrm{Al}}$ = aluminum elemental species
e-a = electron and neutral atom
e-i = electron and ions
int = liquid–vapor interface
l = liquid
$\tilde{\mathrm{N}}$ = nitrogen elemental species
sf = surface of aluminum target
t = target
v = vapor
0 = ambient

I. Introduction

MODERN powerful lasers can be used as a remote energy supply to produce the impulse in space propulsion [1,2]. Recent efforts have shown that an ablative laser propulsion, in which laser ablation of solid propellant is used in a propulsive system, is an optimum method to obtain the impulse more efficiently in space [3,4]. In addition, because the ablative impulse can be enhanced in an ambient gas [5,6], there has been a renewed interest in chemical propulsion as a favorable alternative [7] since Kantrowitz first proposed laser propulsion [8]. Those past studies [1–7] have shown that the impulse generation strongly depends on a number of physical parameters, such as laser wavelength, laser intensity and pulse width, ambient gaseous environment, such as gas species or pressure, and target thermophysical characteristics. Therefore, a detailed understanding of the impulse generation mechanisms during the laser ablation processes will be necessary to design an optimum ablative laser propulsive system.

Very recently, the time variation of the surface pressure generated on a target irradiated pulsed-laser beam was measured [9]. In the measurement, the velocity of the back-surface target in motion is measured based on a velocity interferometer called the Velocity Interferometer System for any reflector (VISAR) [9]. The local impulse is evaluated by integrating the pressure on the local surface of the target. The time resolution of the measured data is about 4 ns. Further details are given in Anju et al.'s paper [9] and are omitted here. Measurements are carried out using the neodymium: yttrium aluminum garnet (Nd:YAG) laser with a laser wavelength of 1064 nm. An aluminum foil is used as target material. The laser condition is summarized in Table 1. The experiment is conducted in a test chamber filled with air. The ambient pressure is changed from 10^{-2} to 10^{5} Pa. However, a thorough understanding of the time-resolved impulse data is believed to be insufficient. The insufficiency would seem to stem from the lack of quantitative information such as the flow properties in the transient flowfield during the order of a nanosecond. By obtaining such quantitative information, a whole

---

Presented as Paper 1080 at the 46th AIAA Aerospace Sciences Meeting and Exhibits, Reno, NV, 7–10 January 2008; received 28 March 2008; accepted for publication 4 September 2008.

*Associate Professor, Department of Aerospace Engineering. Member AIAA.

Table 1 Nd:YAG laser condition

Parameter	Value
Laser wavelength, nm	1064
Laser energy, J	0.9
τ_{FWHM}, ns	9
Laser diameter, mm	2.8

aspect of the mechanisms of the impulse generation with laser ablation could be better understood.

By using a computational technique, one can expect that the transient flowfield structure can be clarified in more detail. For this purpose, the relevant physics with laser ablation needs to be implemented in a numerical method; a heating process within a target material during the irradiation of the laser pulse must be calculated by accounting for the gasification process, including melting and evaporation, and for the reflection of the laser beam at the surface of the target; the dynamics of the expanding ablation jet and the interaction with ambient gas must be computed in a time-dependent manner by accounting for the incident and reflected laser radiation transfer. Even though such a computational approach is widely used (see, e.g., Bogaerts et al. [10]), the problem is essentially ill-posed; for example, it is difficult to know the laser beam reflectivity at the target surface during the irradiation of the laser beam, and the behavior of the computed flowfield is totally different for the different reflectivity value. Therefore, the computational technique must be validated before it can be used.

The aim of the present study is to investigate the impulse generation mechanisms through the laser ablation of an aluminum target irradiated with the Nd:YAG laser. A computational method is used to diagnose the experimental results of the real-time impulse data obtained by using the VISAR [9]. The laser ablation phenomenon is simulated for the ambient pressure conditions in the experiment by using the computational method. The computational method is validated at first against the measured time-resolved impulse data, showing the comparison of the impulse history between the measurement and calculations for the different ambient pressures. Next, the transient behaviors of the laser energy absorption processes, and the properties in a flowfield during and after the laser power peak, are examined to understand the mechanisms of the laser-ablative impulse generation on the aluminum foil.

This author has recently calculated the experimental condition only for $p_0 = 10^{-2}$ Pa by using a computational approach [11]. The computational fluid dynamics (CFD) method used incorporates the physical modeling related to laser ablation. In the previous method, the ambient gas is assumed to be an inert gas. As the ambient pressure becomes higher, a shock wave is formed due to the laser ablation of the aluminum target. The laser beam could be absorbed by the high-temperature gas behind the shock wave so produced, leading to the different behavior of the impulse generation. Such a laser absorption process cannot be examined by using the previous method. Therefore, in the present study, a plasma model is newly incorporated into the previous computational method to simulate a possible laser absorption by the ambient gas; a dissociation and ionization equilibrium model is used to describe a plasma state and radiation absorption coefficients.

II. Numerical and Physical Modeling

To calculate the time variation of the local impulse generated on the aluminum target irradiated by a nanosecond pulse laser, both the dynamics of the expanding aluminum vapor produced by the laser ablation and the heat conduction in the target, including melting and vaporization, are simulated simultaneously. The coordinate system in the present method is given in Fig. 1. Although the CFD technique employed in the present study is mostly retained from the methodology used in the previous analysis [11], the method will be briefly explained for completeness.

A. Flowfield

The expansion processes of the aluminum vapor produced by laser ablation are calculated using a computational fluid dynamics technique. The one-dimensional flowfield is assumed to be inviscid. Mass of the vaporized aluminum and of the ambient gas, momentum, and energy conservation equations are solved. The total density in a point in a flowfield is given by the sum of each of the densities for the vaporized aluminum and the ambient gas. The equations are discretized using a finite volume method. The discretized equations are numerically integrated in time by using an Euler explicit method. The numerical flux function is evaluated using the AUSM-DV scheme [12] with the MUSCL approach. Computed flow properties are second-order accurate in space and first-order in time, respectively. The size of a global time step is typically on the order of 10^{-12} s in the present study; this value is believed to be adequate to examine the unsteady flow phenomenon during the order of a nanosecond. It should be noted that the time step is determined at each time by comparing the minimum time step given by the stability condition for the heat conduction equation [13] and the Courant–Friedrichs–Lewy (CFL) condition for flowfield. The CFL number is set to be 0.1. For the boundary condition at the target surface, the numerical flux function is given by specifying the vapor properties. These properties will be explained later.

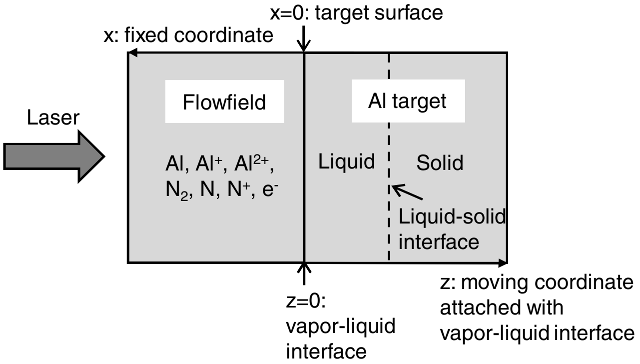

Fig. 1 Schematic diagram of the coordinate system for laser ablation processes.

A high-temperature thermochemical state of the gas mixture is determined by assuming a local thermodynamic equilibrium (LTE) state. Because the VISAR measurement is conducted under air, all the chemical species to be present in high-temperature air need to be accounted for to determine the chemical composition in an LTE state. Such an elaborate approach is possible, but an efficient procedure is required to reduce the computing time of the portion for the thermochemical equilibrium calculation. Such a tedious procedure is avoided in the present study, and the possible species in high-temperature air are represented by including only the nitrogen species shown as follows. The effect of neglecting the oxygen-bearing species on the computed solutions is small, and this point will be discussed later.

Seven chemical species (N_2, N, N^+, Al, Al^+, Al^{2+}, and e) are accounted for. The following equations are solved to calculate species number densities in an equilibrium state:

$$2n_{\mathrm{N_2}} + n_{\mathrm{N}} + n_{\mathrm{N^+}} = n_{\tilde{\mathrm{N}}}$$

$$n_{\mathrm{Al}} + n_{\mathrm{Al^+}} + n_{\mathrm{Al^{2+}}} = n_{\tilde{\mathrm{Al}}}$$

$$n_{\mathrm{N^+}} + n_{\mathrm{Al^+}} + 2n_{\mathrm{Al^{2+}}} = n_{\mathrm{e}}$$

$$\frac{n_{\mathrm{N}}^2}{n_{\mathrm{N_2}}} = \frac{Q_{\mathrm{N}}^2}{Q_{\mathrm{N_2}}}\exp\left(-\frac{D_{\mathrm{N_2}}}{kT}\right)$$

$$\frac{n_{\mathrm{N^+}}n_{\mathrm{e}}}{n_{\mathrm{N}}} = \frac{Q_{\mathrm{N}}Q_{\mathrm{e}}}{Q_{\mathrm{N}}}\exp\left(-\frac{I_{\mathrm{N}}}{kT}\right)$$

$$\frac{n_{\mathrm{Al^+}}n_{\mathrm{e}}}{n_{\mathrm{Al}}} = \frac{Q_{\mathrm{Al^+}}Q_{\mathrm{e}}}{Q_{\mathrm{Al}}}\exp\left(-\frac{I_{\mathrm{Al}}}{kT}\right)$$

$$\frac{n_{\mathrm{Al^{2+}}}n_{\mathrm{e}}}{n_{\mathrm{Al^+}}} = \frac{Q_{\mathrm{Al^{2+}}}Q_{\mathrm{e}}}{Q_{\mathrm{Al^+}}}\exp\left(-\frac{I_{\mathrm{Al^+}}}{kT}\right)$$

The partition function is evaluated in the way given in [14]. The internal energy is given by [14]

$$\epsilon = \frac{5}{2} n_{N_2} kT + \frac{3}{2}(n_{N} + n_{N^+} + n_{Al} + n_{Al^+} + n_{Al^{2+}})kT + \frac{3}{2} n_e kT + \epsilon_D + \epsilon_I$$

Because the internal energy is a function of both of species number density and temperature, an iterative method is used to calculate a local thermodynamic equilibrium temperature by simultaneously solving the preceding equations. It should be noted that most of the flowfield analyzed in the present study is in a high-temperature state except for the narrow region near a shock wave. Thus, in the high-temperature flowfield region, where the effect of the dissociation of N_2 is negligibly small, the contribution of N_2 is removed in the preceding formulation.

The thermal radiation process is represented by the continuum radiation, which consists mainly of free–free transition [10]. The total amount of energy emitted by the free–free transition is calculated by the formula given by Spitzer [15]. The absorption coefficient is given by the sum of the contributions from the inverse Bremsstrahlung processes between electron and neutral atomic species, and between electron and ions, as follows [16]:

$$\kappa^{IB} = \kappa^{IB}_{\text{e-a}} + \kappa^{IB}_{\text{e-i}}$$

$$\kappa^{IB}_{\text{e-a}} = \left\{1 - \exp\left(-\frac{hc}{\lambda kT}\right)\right\} n_{e^-}(n_N + n_{Al}) Q_c$$

$$\kappa^{IB}_{\text{e-i}} = \left\{1 - \exp\left(-\frac{hc}{\lambda kT}\right)\right\} \frac{4e^6\lambda^3}{3hc^4 m_e}\left(\frac{2\pi}{3m_e kT}\right)^{\frac{1}{2}} n_e(n_{N^+} + n_{Al^+} + 4n_{Al^{2+}})$$

where Q_c denotes the averaged cross section for a collision between electron and a neutral atom. The Q_c value is taken from [16] and is set to be 10^{-36} cm^5 in the present calculation. This value is nearly the same as the experimental value given by Taylor and Caledonia [17]. However, their data were presented for the wavelength of 2–4 μm. Calculations are made by using both double and half the cross section used in the present study to check the validity of the value used. It is found that the calculated impulse value is not so changed.

The original incident laser intensity is attenuated by the high-temperature plasma. In addition, a certain amount of the incident laser beam could be reflected at the target surface, and the reflected laser beam might be reabsorbed by the expanding plasma. The absorption processes are computed by solving the transfer equation for the incident and reflected laser beam as follows:

$$\frac{\partial I^-}{\partial x} - \kappa^{IB} I^- = 0 \qquad \frac{\partial I^+}{\partial x} + \kappa^{IB} I^+ = 0$$

where I^- denotes the incident components of the laser beam, and I^+ denotes the reflected components, respectively. The total laser intensity at a point in a flowfield is given by the sum of the two components $I = I^+ - I^-$. To calculate the laser energy transfer equations, the boundary condition is set to be as follows: the laser intensity for the far-field boundary at $x = \infty$ is given by the original laser intensity, and the intensity for the target boundary at $x = 0$ is given by $R_{sf} I^-$. The radiation source term so calculated is included in the energy equation.

It should be noted that all of the present calculations show that the electron number density is below 10^{27} m^{-3}, which is a critical number density for the laser cutoff with the 1064 nm Nd:YAG laser, as will be seen in a later section. Therefore, the cutoff phenomenon for the Nd:YAG laser is neglected in the present computational method.

Table 2 Thermophysical parameters for aluminum

Parameter	Value
Specific heat of liquid, J/(kg · K)	2229
Specific heat of solid, J/(kg · K)	901
Melting temperature, K	934
Normal boiling temperature, K	2740
Latent heat of fusion, kJ/mol	10.3
Latent heat of vaporization at normal boiling point, kJ/mol	288.3
Thermal conductivity of liquid, W/(m · K)	100
Thermal conductivity of solid, W/(m · K)	225
Density of liquid, kg/m^3	2700
Density of solid, kg/m^3	2700
First ionization energy, eV	5.99
Second ionization energy, eV	18.83

B. Heat Conduction in Aluminum Target and Vaporization

A one-dimensional heat conduction equation is solved to calculate the pulsed-laser heating of an aluminum target [10]. The phase transition, such as melting and evaporation, is accounted for. The heat conduction equation can be written as

$$\frac{\partial H_t}{\partial t} - v_{\text{int}} \frac{\partial H_t}{\partial z} = \frac{\partial}{\partial z}\left(\kappa_t \frac{\partial T_t}{\partial z}\right)$$

where z is the moving coordinate attached to a liquid–vapor interface. The temperature within the target is evaluated by assuming that the enthalpy H_t is a function of temperature. The thermophysical parameters, such as specific heat, thermal conductivity, and density for solid and liquid, respectively, are assumed to be temperature independent. The thermophysical parameters of aluminum used in the present study are summarized in Table 2. The equation is discretized using a finite volume method. Solutions are obtained by integrating the discretized equation using an explicit method. The adiabatic condition is specified at $z = \infty$. The boundary condition at $z = 0$, which denotes the heated surface, is given by

$$\left(\kappa_t \frac{\partial T_t}{\partial z}\right)_{z=0} = \rho_l \Delta H_v v_{\text{int}} - (1 - R_{sf}) I^-_{x=0}$$

It should be noted that, because the absorption length of the laser incident on the target is on the order of 10^{-7} m for the case considered in the present study, the penetration of the laser within the aluminum target is neglected and the laser energy is assumed to be completely absorbed at the surface of the target [18].

An effective reflectivity value is used to account for the reflection of the incident laser beam at the target surface, in which the reflectivity value is taken to be constant in the calculation. This procedure is used because it is difficult to determine the reflectivity value correctly including melting and evaporating during nanoseconds. It is shown in previous work [11] for the case of $p_0 = 10^{-2}$ Pa that the impulse increases when the surface reflectivity value is decreased, and that the time history of the impulse data is reproduced by choosing the reflectivity value appropriately. Note that the appropriate reflectivity value used in the present study is slightly higher than the one used in the previous method [11]. It is believed that the difference comes from the different approach taken in the present study for the modeling of laser radiation transfer; the reflected laser energy transfer was ignored in the previous study.

The velocity of the liquid–vapor interface is determined from the flux of atoms leaving from the interface as follows:

$$v_{\text{int}} = \frac{p_v}{\rho_l (2\pi k T_{sf}/m)^{\frac{1}{2}}}$$

The vapor pressure p_v can be calculated by using the Clausius–Clapeyron equation with the surface temperature T_{sf}:

$$p_v = p_0 \exp\left\{\frac{\Delta H_v (T_{sf} - T_{bp})}{R_g T_{sf} T_{bp}}\right\} \tag{1}$$

where p_0 is 1.013 MPa.

For the ablating surface, the boundary condition for the flowfield calculation is given by the solution for the heat conduction equation. The vapor density, velocity, and pressure values at the evaporating surface are calculated as a function of the temperature at the surface of the target. The vapor pressure is given by Eq. (1). The vapor density is calculated through an equation of state:

$$\rho_v = \frac{p_v m}{k T_{\mathrm{sf}}}$$

The velocity of the vapor evaporated from the target surface is given by the mass conservation relation at the surface as follows:

$$\rho_v v_v = \rho_l v_{\mathrm{int}}$$

The total enthalpy of the vapor is determined from the relation of the energy conservation, assuming that the velocity of the liquid aluminum is negligibly small. When no vaporization occurs, the target surface is assumed to be adiabatic.

Other conditions are given as follows. Initial temperature values in the flowfield and in the target are taken to be 300 K, respectively. Calculations are carried out by using two grids in the flowfield: 401 and 801 grid points. The sensitivity of the computational grid to the calculated flow properties becomes about 3% at most between the two grid points. Thus, the results are presented by using the finer (801) grid. The grid size is set nonuniformly by specifying the minimum spacing adjacent to the target boundary to be 250 nm. For the heat conduction within the aluminum target, the number of 1001 grid points with the uniform spacing of 20 nm is used.

III. Results and Discussion

A. Validation of Computational Method by Comparing with Time-Resolved Impulse Characteristics

In Fig. 2, the temporal variation of the impulse is plotted against elapsed time from the onset of the laser irradiation. Both the measured and calculated impulse data are given for $p_0 = 10^{-2}$ Pa, 40 kPa, and 100 kPa, respectively. In the calculation, the impulse value is evaluated by integrating the computed pressure at the computational cell adjacent to the target boundary with time. The calculated results are presented for the surface reflectivity value R_{sf} with 0.72. In addition, the results with $R_{\mathrm{sf}} = 0.3$ and 0.9 are given, especially for the case of $p_0 = 10^{-2}$ Pa, for the purpose of comparison.

From the comparison of the calculated results with the different reflectivity values for the case of $p_0 = 10^{-2}$ Pa, the impulse is very sensitive to the reflectivity value chosen; calculation predicts a higher impulse as the reflectivity value is decreased. This trend is because the laser energy is absorbed more intensely at the target. As a result, the aluminum target is strongly ablated, leading to the higher impulse value. As shown, calculation with $R_{\mathrm{sf}} = 0.3$ overestimates the measured time-resolved impulse data and underestimates with $R_{\mathrm{sf}} = 0.9$. Calculation predicts the measured temporal variation of the impulse fairly well when setting the R_{sf} value to be 0.72.

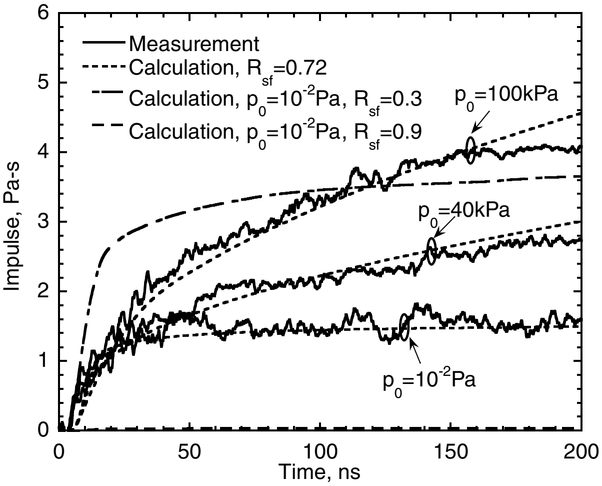

Fig. 2 Comparison of time history of local impulse between measurement and calculations for different ambient pressure conditions.

From the comparison of the data between the measurement and calculations for the higher ambient pressure cases of $p_0 = 40$ k and 100 kPa, it is found that the overall feature of the measured temporal variation of the impulse is reproduced when R_{sf} is taken to be 0.72. In contrast to the case of $p_0 = 10^{-2}$ Pa, one can see that the impulse is still increased after about $t = 30$ ns. The behavior of the impulse history is different between two higher ambient pressures, and the different behavior is replicated by the present calculation.

It should be noted that the constant reflectivity value is not likely to occur during subpicoseconds after the onset of the laser irradiation [19]. However, the validity of the present calculation is warranted within the time resolution of the VISAR data (4 ns). Thus, the analysis using such a variable reflectivity with time is beyond the scope of the present work.

The effect of the reflected laser energy absorption on the impulse history is larger for $p_0 = 100$ kPa as compared with other conditions. In a realistic experimental condition, the incident laser beam will not be specularly reflected, but might be diffusively reflected, because the target surface will be disrupted by the laser irradiation. Nevertheless, the simulated result is likely to occur; the reflected laser energy is absorbed within a very narrow distance compared with the diameter of the laser pulse, as will be shown later. When the reflected laser beam absorption is ignored, the present calculation underestimates the measured impulse history consistently until about $t = 170$ ns by 10% for the case of $p_0 = 100$ kPa. This underestimation can be reduced by setting the surface reflectivity value to be lower than a value of 0.72. However, the time variation of the impulse for $p_0 = 10^{-2}$ Pa and 40 kPa cannot be reproduced when using this lower reflectivity value. Because the temperature at the target is about 6000 K at most for the ambient pressure conditions analyzed in the present study, the surface reflectivity value should be nearly the same. Therefore, the obtained agreement between measurement and calculation accounting for the absorption of the reflected laser energy with a single reflectivity value is believed to be reasonable.

One can see from Fig. 2 that calculation overestimates the measured impulse after $t = 150$ ns for the case of $p_0 = 100$ kPa. The cause of the discrepancy is likely due to the two-dimensional effect. When expansion waves from the periphery of the laser spot reach the centerline, the pressure on the centerline is reduced [20]. Because one-dimensional flow is assumed in the present method, the pressure decrease due to the two-dimensional expansion wave is not simulated. As a result, the present calculation will tend to overestimate the experimental impulse data after the expansion wave reaches the centerline region. By dividing the radius of the laser spot by the sound speed of the plasma, the timescale before the expansion waves arrive at the centerline can be evaluated [20]. Based on the calculated flow solutions, the evaluated time is about 220, 200, and 130 ns for the cases of $p_0 = 10^{-2}$ Pa, 40 kPa, and 100 kPa, respectively. The timescales for $p_0 = 10^{-2}$ Pa and 40 kPa confirm the observed result in Fig. 2; a good agreement of the data is seen during 200 ns, showing that one-dimensional assumption is valid. Thus, in the next section, the calculated transient flowfield will be examined less than the timescale so estimated.

B. Impulse Generation Mechanisms

1. Laser Beam Absorption by the Plasma

In Fig. 3, the laser intensity profiles incident to the aluminum target are plotted against elapsed time for $p_0 = 10^{-2}$ Pa, 40 kPa, and 100 kPa, respectively. In the figure, the profile denoted by "without absorption" is taken from the experimental laser output measured using a photon detector. From the calculated intensity profiles, one can see that the intensity is reduced at $t = 5$ ns for all cases analyzed in the present study. Such a trend continues during the duration time of the laser pulse. The reduction is due to the so-called plasma shielding effect. The behavior of the laser absorption processes is different between the three ambient pressure conditions, leading to different impulse generation mechanisms, as will be explained next.

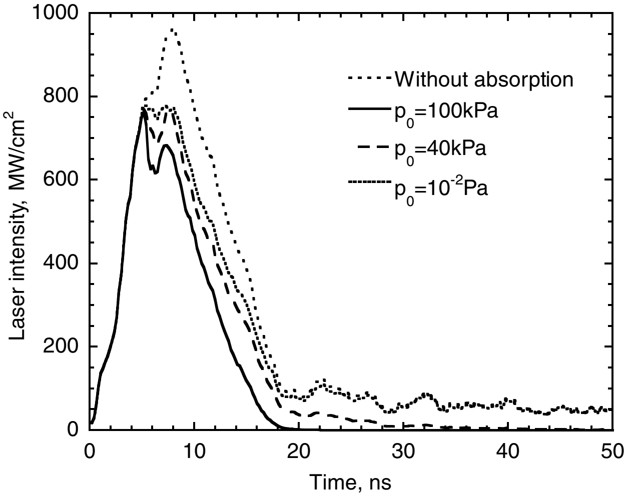

Fig. 3 Temporal variation of calculated incident laser intensity on target surface for different ambient pressure conditions.

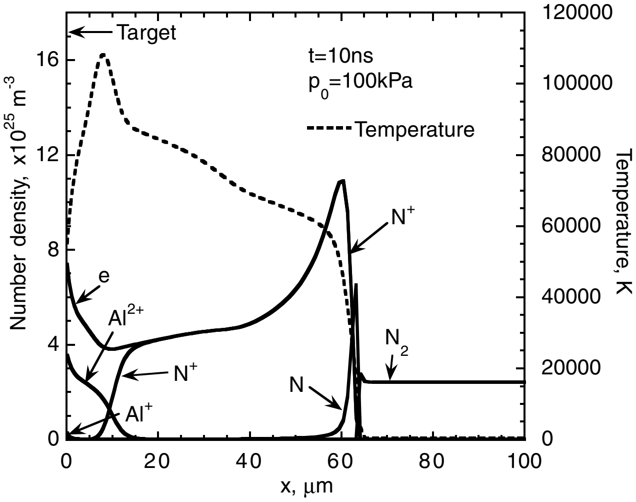

Fig. 4 Spatial distribution of calculated species number density at $t = 10$ ns for $p_0 = 100$ kPa.

2. $p_0 = 100$ kPa

The spatial distribution for the calculated species number densities and temperature is plotted, respectively, at $t = 10$ ns in Fig. 4. From the figure, it is found that the ablated vapor is confined within $x = 10\ \mu$m from the target. The temperature therein is between 60,000 and 115,000 K. As a result, the vapor is in an ionized state: the dominant species are Al^{2+} and electron. A shock wave is seen at nearly $x = 60\ \mu$m. The shock wave is formed as a result of the compression of the ablated vapor. The temperature behind the shock wave becomes about 40,000 K; molecular nitrogen is dissociated and ionized to form N, N$^+$, and electron.

Figure 5 shows the spatial distributions of the computed laser intensity and the inverse Bremsstrahlung absorption coefficients at $t = 10$ ns. In the figure, the incident and reflected laser intensity profiles are given. One can see that the incident laser energy is strongly absorbed by about 20% in the narrow region behind the shock wave, showing the breakdown of the ambient gas. The strong absorption is due to the electron-neutral inverse Bremsstrahlung processes, followed by the dissociation and ionization of molecular nitrogen. Based on the absorption characteristics shown in the figure, the flowfield is believed to be in the regime of so-called laser supported detonation [16]. It should be noted that the laser penetrates into the target during the duration of the laser pulse. As shown, the reflected laser energy is absorbed within a distance that corresponds to about 2% of the diameter of the laser pulse (2.8 mm) for this case.

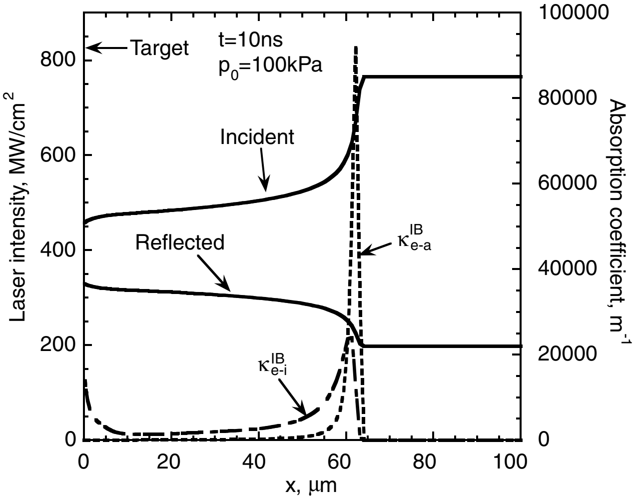

Fig. 5 Spatial distribution of laser intensity and absorption coefficients at $t = 10$ ns for $p_0 = 100$ kPa.

Figure 6 shows the spatial distributions of the calculated pressure and vapor and ambient density, respectively. The results are presented at $t = 10$, 20, and 60 ns. The pressure increase behind the shock wave seen at $t = 10$ ns is a result of the absorption of laser energy shown in Fig. 5. The laser energy absorption therein continues during the laser pulse. From the density distribution at

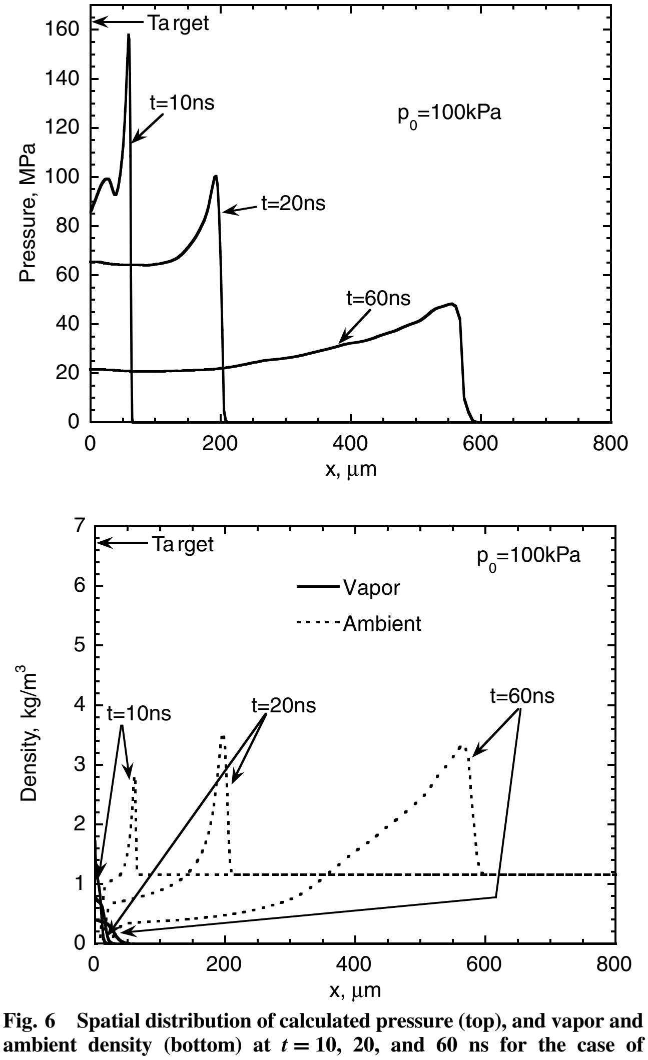

Fig. 6 Spatial distribution of calculated pressure (top), and vapor and ambient density (bottom) at $t = 10$, 20, and 60 ns for the case of $p_0 = 100$ kPa.

$t = 20$ ns, one can see that the ablated aluminum vapor remains in nearly the same region on the target even at this time. This trend, in turn, keeps a relatively higher pressure near the target surface, resulting in higher local impulse generation for this case, as shown in Fig. 2. After the laser power peak, because the flowfield behind the shock wave is relaxed nearly isentropically during that period, the surface pressure value is decreased depending on the pressure behind the shock wave [20]; the surface pressure value at $t = 60$ ns is only one-fourth the one at $t = 10$ ns. This feature leads to impulse generation after the duration time for the case of $p_0 = 100$ kPa observed in Fig. 2.

Based on the calculated result for $p_0 = 100$ kPa, the temperature becomes so high that N produced by the dissociation of N_2 ionizes very quickly. In addition, the dissociation reaction is significant in a relatively narrow region behind the shock wave. It should be noted that the dissociation energy of O_2 is lower than that of N_2, and the ionization energy of O is nearly the same as that of N. As a result, in the high-temperature regime calculated in the present study, O_2 will be fully dissociated, and O so produced is believed to be totally ionized, as in the case of N. Moreover, the cross section value for electron-neutral inverse Bremsstrahlung processes is nearly the same between N and O. Therefore, the effect of oxygen-bearing species on the computed impulse history is believed to be small for the cases analyzed in the present study.

As explained earlier, the present calculation indicates that the high-temperature gas is transparent up to the target during the duration of the laser pulse. Additional calculation is carried out by accounting for double ionized nitrogen to examine whether the transparent nature of the high-temperature plasma is altered. The result shows that the incident laser energy is absorbed by about 50% up to the target, whereas the difference of the calculated impulse value is about 4% at most. Therefore, even though the laser absorption behavior could be affected by accounting for multiple-charge ionization of nitrogen, the effect of the impulse generation is likely to be small.

3. $p_0 = 40$ kPa

The results are similarly presented for the case of $p_0 = 40$ kPa. The calculated species number densities and temperature distributions at $t = 10$ ns are given in Fig. 7, and the calculated laser intensity and absorption coefficients are shown in Fig. 8, respectively. From Fig. 7, one can see that the confinement of the ablated vapor becomes weaker as compared with $p_0 = 100$ kPa; the interface between the ablated vapor and the ambient gas is seen nearly at $x = 30$ μm. The temperature of the aluminum vapor therein is about 40,000–110,000 K. A shock wave is seen at nearly $x = 60$ μm. The dissociation and ionization occurs behind the shock wave, resulting in the formation of N and N^+ species.

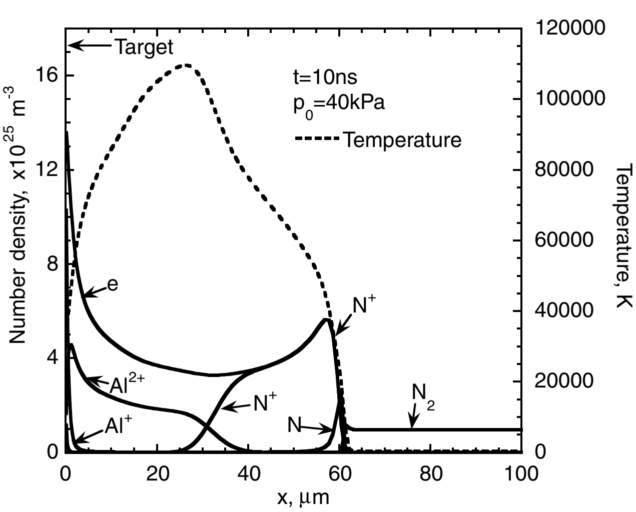

Fig. 7 Spatial distribution of calculated species number density at $t = 10$ ns for $p_0 = 40$ kPa.

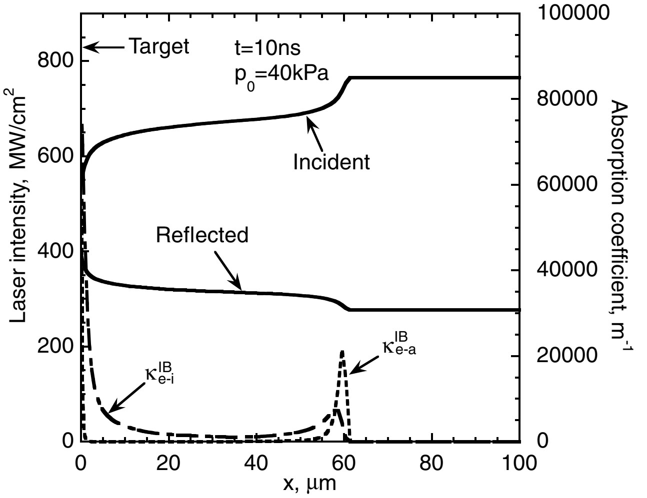

Fig. 8 Spatial distribution of laser intensity and absorption coefficients at $t = 10$ ns for $p_0 = 40$ kPa.

However, one can see from Fig. 8 that the laser energy is absorbed by only about 5% right behind the shock wave. The laser energy is absorbed more strongly by the high-temperature aluminum vapor by nearly 20%. The trend is opposite to the case of $p_0 = 100$ kPa.

Figure 9 shows the spatial distributions of the calculated pressure and vapor and ambient density, respectively. From the pressure

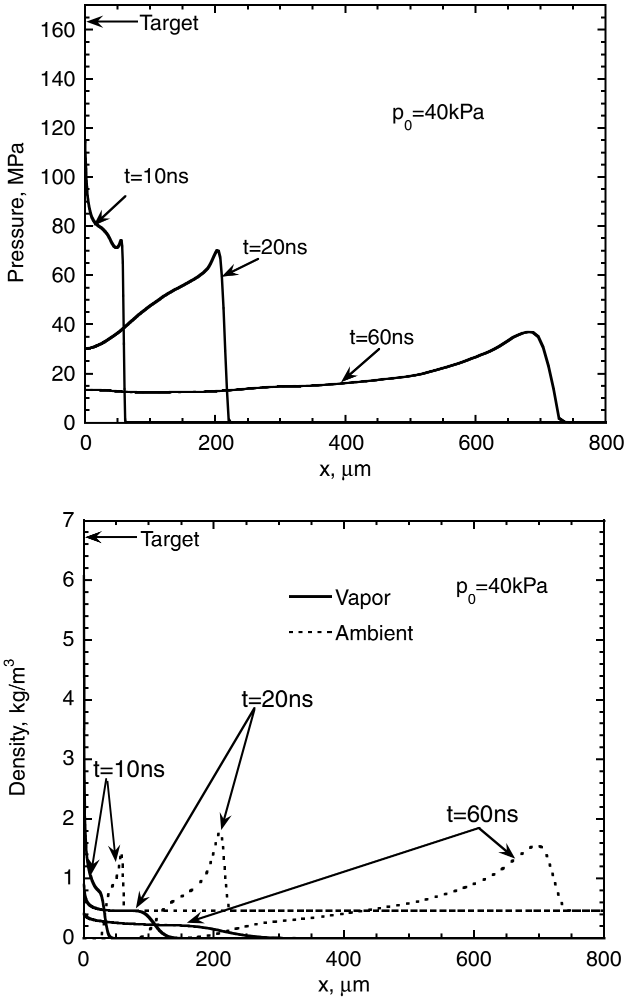

Fig. 9 Spatial distribution of calculated pressure (top), and vapor and ambient density (bottom) at $t = 10$, 20, and 60 ns for the case of $p_0 = 40$ kPa.

distribution at $t = 10$ ns, the pressure just behind the shock region increases only slightly because the laser energy is weakly absorbed therein. The pressure at the target surface is about 110 MPa, which is higher than the one just behind the shock wave by a factor of 1.5. From the density distribution at $t = 20$ ns, the aluminum vapor expands and its front moves nearly up to $x = 100$ μm, while the expansion of the vapor is restricted by the ambient gas. As a result, the pressure of the ambient gas behind the shock wave increases by the compression of the vapor; in contrast, the pressure at the target surface is decreased by the rarefaction of the aluminum vapor. After the laser pulse, even though the target pressure is decreased as in the case of $p_0 = 100$ kPa, it is still high enough to generate the impulse on the target, as was seen in Fig. 2. Note that the lower impulse generation for $p_0 = 40$ kPa is likely due to the different processes observed in the region behind the shock wave during the laser pulse between $p_0 = 40$ and 100 kPa.

4. $p_0 = 10^{-2}$ Pa

The results are summarized similarly in Figs. 10–12 for the case of $p_0 = 10^{-2}$ Pa. From Fig. 10, for the computed number density and temperature at $t = 10$ ns, the temperature is about 30,000–80,000 K, and Al^{2+} and electron are the dominant species therein. The tip of the vapor reaches about $x = 140$ μm at this time, although the position is out of the scale in Fig. 10. From Fig. 11, the incident laser beam is absorbed by 23% within about 80 μm away from the target. The reflected laser beam is absorbed in the same region. The absorption coefficient for electron-ion inverse Bremsstrahlung dominates in the region near the target, as shown in Fig. 11.

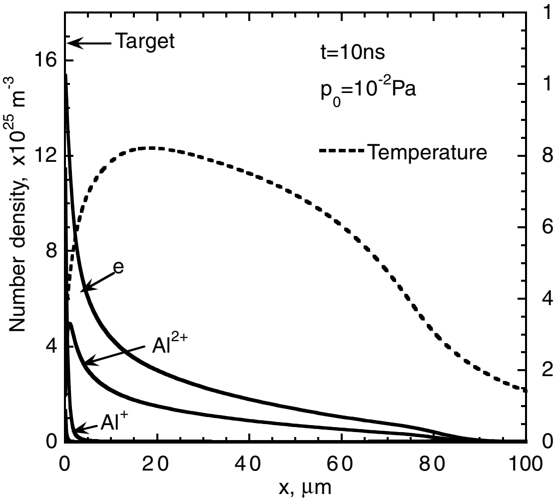

Fig. 10 Spatial distribution of calculated species number density at $t = 10$ ns for $p_0 = 10^{-2}$ Pa.

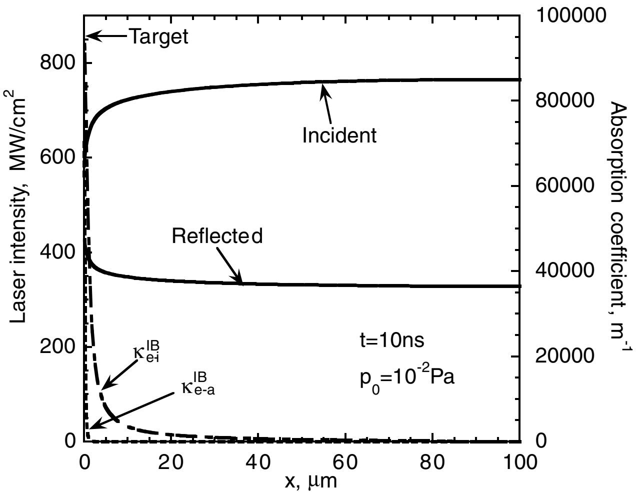

Fig. 11 Spatial distribution of laser intensity and absorption coefficients at $t = 10$ ns for $p_0 = 10^{-2}$ Pa.

The calculated pressure and density distributions at $t = 10$, 20, and 30 ns are presented in Fig. 12, respectively. The surface pressure value at $t = 10$ ns is about 133 MPa, which is higher toward the target. The surface pressure is reduced to about 7 MPa until $t = 30$ ns. For this nearly vacuum case, the aluminum vapor expands rapidly during 30 μs, as can be seen in the density distribution; the expansion velocity of the vapor is about 50,000 m/s at the tip of the aluminum vapor, although the result is not shown here. The momentum of the aluminum vapor produces the impulse on the target at only about 30 ns, as shown in Fig. 2.

C. Calculated Evaporated Depth of Aluminum Target

The calculated evaporated depth is evaluated by $v_{\text{int}} \times t$. The calculated data are presented in Fig. 13 for $p_0 = 100$ kPa, 40 kPa, and 10^{-2} Pa. As shown, the evaporation starts from about $t = 5$ ns for all cases. The calculated evaporation slows down to zero later as the ambient pressure decreases based on the calculated data; the evaporation ends at about $t = 9$ ns for $p_0 = 100$ kPa, at about $t = 15$ ns for $p_0 = 40$ kPa, and at about $t = 18$ ns for $p_0 = 10^{-2}$ Pa. The calculated result is related to the unsteady flowfield behavior shown earlier for each of the cases calculated: for $p_0 = 10^{-2}$ Pa, the evaporating time is the same as the laser duration time ($=2\tau_{\text{FWHM}}$), which is nearly equal to that of the impulse generation; for

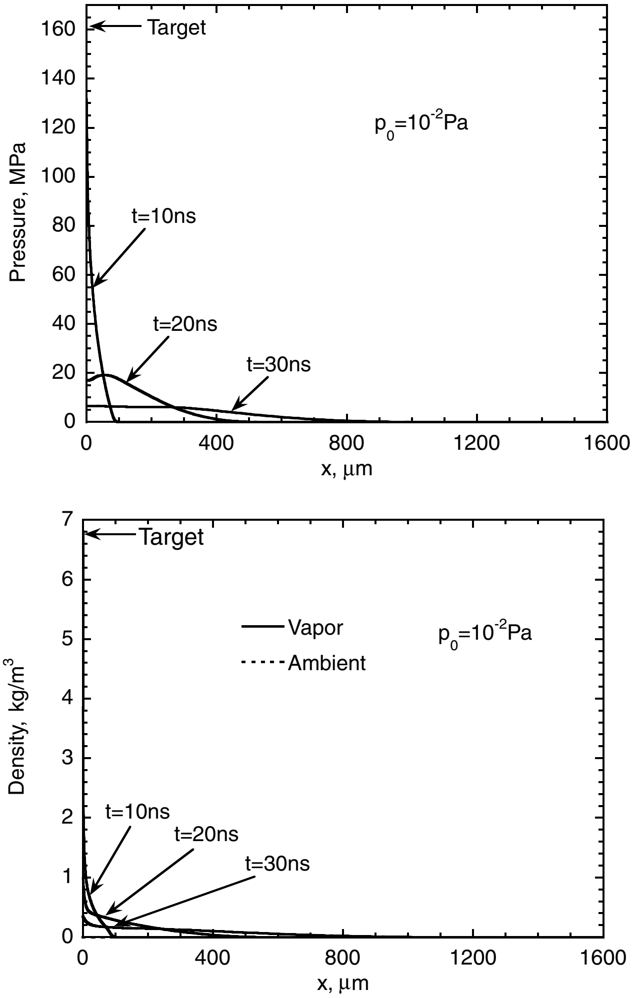

Fig. 12 Spatial distribution of calculated pressure (top), and vapor and ambient density (bottom) at $t = 10$, 20, and 30 ns for the case of $p_0 = 10^{-2}$ Pa.

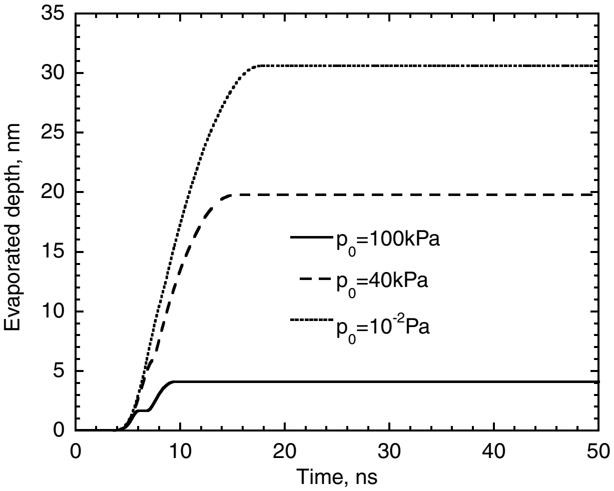

Fig. 13 Temporal variation of calculated evaporated depth for different ambient pressure conditions.

$p_0 = 40$ kPa, the ablating period is shortened due to the plasma-shielding effect added by the ambient gas; and, for the case of $p_0 = 100$ kPa, the ablation continues for the relatively shorter period of τ_{FWHM} due to moderate breakdown of the ambient gas.

In Fig. 14, the evaporated depth is plotted against the ambient pressure. The data are presented for the cases of 10^{-2} to 10^5 Pa. The results for $p_0 = 100$ Pa, 500 Pa, and 10 kPa are presented additionally for reference. For the cases of the relatively lower ambient pressure condition from $p_0 = 10^{-2}$ to 500 Pa, the amount of evaporated depth is almost the same. Calculation shows that there is no discernible difference of the temporal variation of the impulse between these lower ambient pressure conditions, although the result is not shown here. From this observation, one can also deduce the fact that the impulse generation is only dependent on the momentum transfer from the ablation jet for these conditions. It is seen from the figure that the evaporated depth decreases relatively rapidly as the ambient pressure becomes higher from 10kPa to 100 kPa.

Unfortunately, no measured data are available for the experimental conditions analyzed in the present study. Based on the estimation under the one-dimensional assumption made in the present study, the calculated mass loss is about 0.5 μg for the case of $p_0 = 10^{-2}$ Pa. In an aluminum ablation experiment, using the Nd: YAG laser with 532 nm [21], the measured mass loss is about 0.05–0.2 μg under the fluence between 4.4 and 13.7 $\mathrm{J/cm^2}$ at the ambient pressure of 0.04 Pa. When an aluminum target is irradiated by using a pulsed CO_2 laser under conditions with a fluence of 4000 $\mathrm{J/cm^2}$ and an ambient pressure of about 0.1 Pa, the measured mass loss is about 25 μg. The calculated value in the present study is roughly comparable to these measured values. In addition, based on the laser ablation experiment with the CO_2 laser [6], a trend in the sharp change of the material removal rate is observed as the ambient pressure increases from 0.1 Pa to 100 kPa [6]. Such a qualitative trend is consistent with that obtained in the present study.

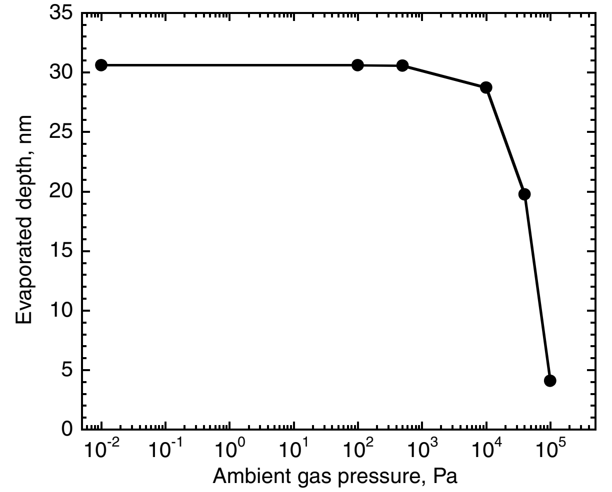

Fig. 14 Comparison of calculated evaporated depth for different ambient pressure conditions.

IV. Conclusions

The impulse generation mechanisms during the interaction of the Nd:YAG laser pulse with the laser wavelength of 1064 nm with an aluminum target are explained by using the computational method. The present computational method is validated by using the measured time-resolved impulse data. The present method accounts for the processes of the laser energy absorption by an ablated aluminum vapor and ambient nitrogen plasma. This calculation suggests the following aspects related to the impulse generation during the laser ablation experiment: When the ambient pressure is 100 kPa, the breakdown of the ambient gas mostly contributes to the impulse generation and the obtained impulse is highest between the cases analyzed in the present study. For $p_0 = 40$ kPa, the confinement of the ablation jet by the ambient gas attributes for a longer impulse generation after the duration time. The effect of the breakdown of the ambient gas is weaker compared with the case of $p_0 = 100$ kPa. For the lower ambient pressure condition of $p_0 = 10^{-2}$ Pa, the impulse is generated by the momentum of the aluminum vapor created during a laser irradiation of the aluminum target. For all cases, the ablated aluminum and the high-temperature ambient gas remain transparent during the primary laser power peak, and the reflected laser energy transfer is attributed to the impulse generation, especially for $p_0 = 100$ kPa. A sharp transition regime from the ablation-dominant to the breakdown-dominant impulse generation is indicated.

Acknowledgments

The author would like to thank Akihiro Sasoh and Koichi Mori (Nagoya University) for their helpful suggestions throughout this work and for providing the experimental data.

References

[1] Pakhomov, A. V., and Gregory, D. A., "Ablative Laser Propulsion: An Old Concept Revisited," *AIAA Journal*, Vol. 38, No. 4, 2000, pp. 725–727.
doi:10.2514/2.1021

[2] Sasoh, A., "Laser-Driven In-Tube Accelerator," *Review of Scientific Instruments*, Vol. 72, No. 3, 2001, pp. 1893–1898.
doi:10.1063/1.1347378

[3] Phipps, C., and Luke, J., "Micropropulsion Using a Laser Ablation Jet," *Journal of Propulsion and Power*, Vol. 20, No. 6, 2004, pp. 1000–1011.
doi:10.2514/1.2710

[4] Pakhomov, A. V., and Gregory, D. A., "Specific Impulse and Other Characteristics of Elementary Propellants for Ablative Laser Propulsion," *AIAA Journal*, Vol. 40, No. 5, 2002, pp. 947–952.
doi:10.2514/2.1731

[5] Watanabe, K., Mori, K., and Sasoh, A., "Ambient Pressure Dependence of Laser-Induced Impulse onto Polyacetal," *Journal of Propulsion and Power*, Vol. 22, No. 5, 2006, pp. 1148–1151.
doi:10.2514/1.22750

[6] Pakhomov, A. V., Lin, J., and Tan, R., "Air Pressure Effect on Propulsion with Transversely Excited Atmospheric CO_2 Laser," *AIAA Journal*, Vol. 44, No. 1, 2006, pp. 136–141.
doi:10.2514/1.11580

[7] Yabe, T., Phipps, C., Aoki, K., Yamaguchi, M., Nakagawa, R., Baasandash, C., Ogata, Y., Shiho, M., Inoue, G., Onda, M., Horioka, K., Kajiwara, I., and Yoshida, M., "Laser-Driven Vehicles: From Inner-Space to Outer-Space," *Applied Physics A: Materials Science and Processing*, Vol. 77, No. 2, 2003, pp. 243–249.

[8] Kantrowitz, A., "Propulsion to Orbit by Ground-Based Lasers," *Astronautics and Aeronautics*, Vol. 10, No. 5, 1972, pp. 74–76.

[9] Anju, K., Sawada, K., Sasoh, A., Mori, K., and Zaretsky, E., "Time-Resolved Measurements of Impulse Generation in Pulsed Laser-Ablative Propulsion," *Journal of Propulsion and Power*, Vol. 24, No. 2, 2008, pp. 322–329.
doi:10.2514/1.32017

[10] Bogaerts, A., Chen, Z., Renaat, G., and Akos, V., “Laser Ablation for Analytical Sampling: What Can We Learn from Modeling?,” *Spectrochimica Acta*, Vol. 58, Pt. B, 2003, pp. 1867–1893. doi:10.1016/j.sab.2003.08.004

[11] Sakai, T., “CFD Simulation of Laser-Ablative Impulse Generation on Aluminum Target,” *Journal of Space Technology and Science*, Vol. 22, No. 2, 2007, pp. 1–10

[12] Wada, Y., and Liou, M. S., “A Flux Splitting Scheme with High-Resolution and Robustness for Discontinuities,” AIAA Paper 94-0083, Jan. 1994.

[13] Hirsch, C., *Numerical Computation of Internal and External Flows*, Fundamentals of Numerical Discretization, Vol. 1, Wiley, New York, 1990, pp. 303–304.

[14] Zel’dovich, Y. B., and Raizer, Y. P., *Physics of Shock Waves and High-Temperature Hydrodynamic Phenomena*, Academic Press, New York, 1966, pp. 176–214.

[15] Spitzer, L., *Physics of Fully Ionized Gases*, Interscience, London, 1956, pp. 147–149.

[16] Root, R. G., “Modeling of Post-Breakdown Phenomena,” *Laser-Induced-Plasmas and Applications*, edited by Rakziemski, L. J., and Cremers, D. A., Marcel Dekker, New York, 1989, pp. 69–103.

[17] Taylor, R. L., and Caledonia, G., “Experimental Determination of the Cross-Sections for Neutral Bremsstrahlung,” *Journal of Quantitative Spectroscopy and Radiative Transfer*, Vol. 9, No. 5, 1969, pp. 681–696. doi:10.1016/0022-4073(69)90014-4

[18] Jeong, S. H., Greif, R., and Rosso, R. E., “Numerical Modeling of Pulsed Laser Evaporation of Aluminum Targets,” *Applied Surface Science*, Vols. 127–129, May 1998, pp. 177–183. doi:10.1016/S0169-4332(97)00629-6

[19] Sokolowski-Tinten, K., Bialkowski, J., Cavalleri, A., Boing, M., Schüler, H., and von der Linde, D., “Dynamics Of Femtosecond Laser Induced Ablation From Solid Surfaces,” *Proceedings of High Power Laser Ablation*, Vol. 3343, International Society for Optical Engineering, Bellingham, WA, 1998, pp. 46–57.

[20] Pirri, A. N., Root, R. G., and Wu, P. K. S., “Plasma Energy Transfer to Metal Surfaces Irradiated by Pulsed Lasers,” *AIAA Journal*, Vol. 16, 1978, pp. 1296–1304.

[21] Mele, A., Giardini Guidoni, A., Kelly, R., Flamini, C., and Orlando, S., “Laser Ablation of Metals: Analysis of Surface-Heating and Plume-Expansion Experiments,” *Applied Surface Science*, Vols. 109–110, Feb. 1997, pp. 584–590. doi:10.1016/S0169-4332(96)00742-8

G. Spanjers
Associate Editor